IPILT-OHPL: An Over-the-Horizon Propagation Loss Prediction Model Established by Incorporating Prior Information into the LSTM-Transformer Structure

Hanjie Ji, *Student Member, IEEE*, Lixin Guo, *Senior Member, IEEE*, Jinpeng Zhang, YiwenWei, *Member, IEEE*, Xiangming Guo, Yusheng Zhang, Tianhang Nie, and Jie Feng

***Abstract*—The evaporation duct is a prevalent atmospheric structure in the marine lower troposphere with significant regional non-uniformity. This structure can trap radio waves inside its layer and enable them to propagate over the horizon with less loss. Therefore, accurately predicting the over-the-horizon propagation loss (OHPL) is important for optimizing the performance of radio-electronic systems. Considering the OHPL characteristics in non-uniform evaporation ducts, this study establishes an OHPL prediction model by incorporating prior information into the LSTM-Transformer structure (IPILT-OHPL). The combination of the LSTM network and Transformer is used to construct the LSTM-Transformer, aimed at leveraging their respective strengths to extract important features of OHPL effectively. In addition, to improve the prediction accuracy, this study incorporates the evaporation duct height as an environmental prior information into the LSTM-Transformer. Finally, this study comprehensively evaluates IPILT-OHPL model performance in different application scenarios. The evaluation results show that the established model not only has high prediction accuracy but also strong generalization ability, which provides a new method for efficiently predicting the OHPL in non-uniform evaporation ducts.**

***Index Terms*—Evaporation duct, long short-term memory (LSTM) network, over-the-horizon propagation loss (OHPL), prediction, Transformer**

I. Introduction

THE evaporation duct is a natural atmospheric refraction structure, which is prevalent in the lower troposphere over marine regions with high humidity and temperature [1]. It is caused by evaporation of seawater. The seawater evaporation increases atmospheric water vapor above the marine surface, causing a swift decline in water vapor levels near the marine surface as height increases, forming an inverse humidity gradient layer [2]. This inverse humidity gradient layer is the evaporation duct.

Furthermore, the evaporation duct can cause abnormal variations of the atmospheric refractivity on the vertical gradient, which will produce abnormal refraction effects on the radio waves [3]. In particular, the refractivity decreases abnormally with height, causing the downward bending of the radio wave propagation trajectory [4]. When this curvature exceeds the curvature of the Earth's surface, the radio waves will be trapped inside the duct layer. Multiple reflections of waves will occur between the upper and lower walls of the duct layer to propagate forward [5]. The evaporation duct height (EDH) serves as an essential parameter for describing the atmospheric refractivity within the evaporation duct. It represents the thickness of the duct-trapping layer, which generally does not exceed 40 m [6].

Therefore, the evaporation duct enables radio waves to propagate over the horizon with less energy loss, thereby extending the effective distance of radio-electronic systems (RES), which contributes to improving the quality of signal transmission [7]. Moreover, due to the variations in meteorological conditions across different marine regions, evaporation ducts over large-scale regions are typically regional and non-uniform [8]. Regional non-uniformity is an inherent property of marine evaporation ducts [9]. The refractivity profiles within the non-uniform evaporation ducts often exhibit significant variations with distance [10].

Accurate OHPL prediction is important for understanding and responding to the performance variations of RES in complex marine environments. According to the predicted results, we can optimize the RES parameters configuration to ensure maximum signal transmission reliability and efficiency [11]. This further ensures that the RES can achieve the best monitoring coverage and effectively use resources. However, compared to normal atmospheric environments, the radio wave propagation characteristics in non-uniform evaporation ducts show obvious anomalies [12], [13], [14], [15]. These anomalies increase the difficulty of accurately predicting the OHPL of radio waves in the evaporation duct.

Since the 21st century, the rapid development of deep learning has promoted the wide application of neural

This Manuscript received January 26, 2024. This work was supported in part by the National Natural Science Foundation of China under Grant U21A20457, Grant 62231021, Grant 62371380, and Grant 62271457; in part by the Stable Support Project of China Electronics Technology Group under Grant A382301194; in part by the Stable Support Project of Basic Scientific Research Institute under Grant A132312217-001. (*Corresponding authors: Lixin Guo; Yiwen Wei.*)

Hanjie Ji, Lixin Guo, Yiwen Wei, Tianhang Nie, and Jie Feng are with the School of Physics, Xidian University, Xi'an 710071, China. (e-mail: jhjxd@stu.xidian.edu.cn; lxguo@xidian.edu.cn; ywwei@xidian.edu.cn; 15125779152@163.com; fengjiecrirp@126.com).

Jinpeng Zhang, Xiangming Guo, and Yusheng Zhang are with the National Key Laboratory of Electromagnetic Environment, China Research Institute of Radiowave Propagation, Qingdao 266107, China. (e-mail: jhjxd@stu.xidian.edu.cn; zhangjp@crirp.ac.cn; xmguo08@163.com; zys1022@sina.com).

Color versions of one or more of the figures in this article are available online at http://ieeexplore.ieee.org

networks. Zhang et al. [16] proposed a prediction model for propagation loss in atmospheric duct using a feedforward neural network (FNN). This FNN-based model takes parameters such as duct parameters and antenna parameters as inputs to predict the propagation loss. Moreover, the FNN-based model prediction accuracy under specific frequency bands can reach more than 90%. Shu et al. [17] proposed a lightweight propagation loss prediction model based on a deep neural network (DNN). The model fully considers the influences of evaporation duct environment and antenna parameters on propagation loss, thus enhancing the applicability of the model in natural scenes. The results show that the model can achieve better prediction performance than k-nearest neighbor, random forest, and linear regression models at different frequencies.

While the above models can accurately predict the OHPL to some extent, they don't consider the temporal relationships of the OHPL. The temporal relationships are very important for OHPL because they reflect the attenuation of radio waves over time during propagation. Unlike regular neural networks, the long short-term memory (LSTM) network is specifically designed for processing temporal data [18], [19]. It realizes the effective management of information flow, and can selectively remember and forget information at different moments through the unique gate mechanism. Therefore, the LSTM network is a suitable method to process the temporal relationships of the OHPL. Ji et al. [20] established a multiscale decomposition prediction model for OHPL based on the LSTM network. They used the variational mode decomposition method to decompose the OHPL into multiple subsequences and then used the LSTM network to build the corresponding prediction models for each subsequence. Finally, the predicted results are obtained by reconstructing the predicted results of subsequences. However, the researchers have studied the combined decomposition prediction methods and indicated some of their shortcomings [21], [22], [23], [24]. Some main shortcomings include large calculations, longer time required for establishing models and prediction, causing information leakage, and reducing the temporal relationships within the subsequence. These shortcomings limit the efficiency and reliability of these decomposition prediction models, making them less applied in practical engineering.

Due to the influence of non-uniform evaporation ducts, the OHPL shows strong local fluctuations, which restricts the efficient learning of temporal relationships of OHPL by the LSTM network. Therefore, it is necessary to improve the ability of the LSTM network to extract and learn local features in OHPL. The Transformer is an Encoder-Decoder architecture designed for processing sequential data [25]. With multi-head attention, parallel processing, and positional encoding, it excels at extracting local features without sacrificing global information. The multi-head attention mechanism enables the Transformer to discern various features, facilitating the extraction of local features.

Therefore, this study uses an LSTM-Transformer structure, obtained by combining the LSTM network and Transformer, to enhance the accuracy of predicting OHPL in non-uniform evaporation ducts. Furthermore, in non-uniform evaporation ducts, the OHPL is directly correlated with the EDH. In this study, by incorporating the EDH as an environmental prior information into the LSTM-Transformer, a novel OHPL prediction model (IPILT-OHPL) is established. The main contributions of this study can be summarized as follows:

1) This IPILT-OHPL model takes full advantage of the Transformer's ability to extract local features, alongside the LSTM network's proficiency in processing temporal relationships. By incorporating EDH as prior information, the model can better cognize the influences of non-uniform evaporation ducts on OHPL, thereby improving the accuracy of the prediction model. Incorporating prior information can facilitate the model better improve interpretability. This is very important for the application of the OHPL prediction model in marine atmospheric environments.
2) This study comprehensively evaluates the IPILT-OHPL model performance by comparing prediction performance and testing generalization ability. The evaluation results show that the comprehensive performance of the IPILT-OHPL model is superior. Its evaluation indicators are superior to other models. Meanwhile, the IPILT-OHPL model has strong generalization ability and can have better predicted results for different OHPLs.
3) The IPILT-OHPL model not only performs well in one-step prediction but also in multiple-step prediction, which is an important aspect overlooked by existing models. Even when the predicted step length is 16, the predicted results of the IPILT-OHPL model are still significantly better than other models. By integrating the feature extraction ability and environmental prior information, the IPILT-OHPL model provides a superior method in the field of OHPL prediction.

The remainder of this study is constructed as follows: Section II presents the modeling of the prediction problem of the OHPL. Section III presents the methods. The data used for this study, including the ERA5 data, measured OHPL data, and measured EDH data are presented in Section IV. In Section V, the establishment process of the IPILT-OHPL model is introduced in detail. Section VI presents the predicted results of the IPILT-OHPL model and other models. The evaluation process and corresponding results of the IPILT-OHPL model are also detailed in this section. Finally, the conclusion is presented in Section VII.

II. Problem Modeling

Since the radio waves propagate forward in uniform evaporation ducts through trapping propagation patterns, the OHPL is closely associated with the propagation distance and the time required for radio wave propagation. The temporal relationships of OHPL at each propagation distance enable it

to predict feature OHPL based on previous OHPL. Therefore, this study considers the temporality of OHPL and performs sequence modeling on it. Considering the OHPL as a time sequence $\{L_t\}$ of length $\tilde{T}$. This time sequence $\{L_t\}$ can be expressed as:

$$\begin{aligned} &\{L_t\} = \{L_1, L_2, ..., L_{\tilde{T}}\} \\ &\text{where } t = 1, 2, ..., \tilde{T} \end{aligned} \tag{1}$$

where L is the OHPL at different moments. The target is to predict the OHPL at future moments based on a known sequence of length T:

$$\begin{aligned} &L_{\tau+T+1}^{pred}, L_{\tau+T+2}^{pred}, ..., L_{\tau+T+h}^{pred} = F(L_{\tau+1}, L_{\tau+2}, ..., L_{\tau+T}) \\ &\text{where } 1 \le \tau \le \tilde{T} - T + 1 \end{aligned} \tag{2}$$

where $L_{\tau+1}, L_{\tau+2}, ..., L_{\tau+T}$ is a known OHPL sequence that constructs the input features of the prediction model and T is also considered as the size of prediction window. Given the known OHPL sequence, $L_{\tau+T+1}^{pred}, L_{\tau+T+2}^{pred}, ..., L_{\tau+T+h}^{pred}$ are the predicted OHPLs in the future and h is the predicted step length. F is the function used to model the prediction method.

III. Methods

A. Naval Postgraduate School Evaporation Duct Model

The evaporation duct model is a common method to obtain the atmospheric refractivity profile and EDH in the evaporation duct. For the radio waves in the frequency range of 100MHz-100GHz, the atmospheric modified refractivity (*M*-profile) can be expressed by the following empirical equation [26]:

$$M(z) = \frac{77.6}{T} \times \left(P + \frac{4810e}{T} \right) + 0.157z \tag{3}$$

where T, P, and e are the atmospheric temperature (AT), atmospheric pressure (AP), and water vapor pressure (WVP), respectively. z is the height above the mean marine surface. According to (3), to calculate the *M*-profile, it is necessary to obtain vertical profiles of AT, AP, and WVP. Based on the Monin-Obukhov similarity theory (MOST) for the atmospheric boundary layer, vertical profiles of AT, AP, and WVP near the marine surface can be calculated by the following equations:

$$T(z) = T(z_{0\theta}) + \frac{\theta_*}{\kappa} \left[\ln\left(\frac{z}{z_{0\theta}} \right) - \psi_\theta \left(\frac{z}{L} \right) \right] - \Gamma_d z \tag{4}$$

$$q(z) = q(z_{0q}) + \frac{q_*}{\kappa} \left[\ln\left(\frac{z}{z_{0q}} \right) - \psi_\theta \left(\frac{z}{L} \right) \right] \tag{5}$$

$$P(z_2) = P(z_1) \exp\left(\frac{g(z_1 - z_2)}{R\overline{T_v}} \right) \tag{6}$$

$$e(z) = \frac{q(z)P(z)}{\varepsilon + (1-\varepsilon)q(z)} \tag{7}$$

where q is specific humidity. θ_* and q_* are scaling parameters of temperature and specific humidity. $z_{0\theta}$ and z_{0q} are the roughness lengths of temperature and specific humidity. κ is the von Karman's constant. ψ_θ is temperature correction function. L is the Monin-Obukhov length. Γ_d is dry adiabatic lapse rate. g is gravity acceleration. R is the gas constant of dry air. $\overline{T_v}$ is the mean value of the virtual temperature at height z_1 and z_2. ε is a constant with a value of 6.22.

This study uses the Naval Postgraduate School (NPS) model to determine the *M*-profile and EDH by diagnostic calculations [27]. Babin [28] and Ivanov [29] extensively analyzed and validated various evaporation duct models, identifying the NPS model as the most reliable. The NPS model employs the Tropical Oceans Global Atmosphere-Coupled Ocean Atmosphere Response Experiment (TOGA-COARE) bulk flux algorithm version 2.6 [30], developed from the TOGA-COARE, for the calculation of scaling parameters of temperature and specific humidity. In addition, the NPS model uses near marine surface AT, AP, wind speed (WS), relative humidity (RH), and sea surface temperature (SST) at the same or different heights to calculate the *M*-profile. When the atmospheric modified refractivity is the smallest at a certain height in the *M*-profile, this height is EDH. Therefore, the NPS model implements the conversion of meteorological variables to EDH. With the development of the TOGA-COARE algorithm version 3.0 [31], this study employs the upgraded TOGA-COARE_3.0 algorithm to calculate temperature and specific humidity scaling parameters to improve the NPS model.

B. Three-Parameter Paulus-Jeske Refractivity Profile Model

To describe the influence of the evaporation duct on atmospheric refractivity, researchers derived simplified evaporation duct refractivity profile models to calculate the *M*-profile. The Paulus-Jeske (PJ) model [32] has been widely used in practical applications because it makes empirical adjustments to unstable conditions. It only uses the EDH parameter to describe the *M*-profile in the evaporation duct. The PJ model has the following logarithmic functional form:

$$M(z) = M_0 + 0.125z - 0.125\delta \ln\left(\frac{z + 0.00015}{0.00015} \right) \tag{8}$$

where M_0 is the modified refractivity of marine surface. δ is EDH. Since the PJ model is only a function of EDH, the shape of the *M*-profile calculated using the PJ model is largely fixed. Douvenot et al. [33] indicated limitations in *M*-profile modeling when using only EDH. The three-parameter PJ model (3-PJ) is a variant based on the "Stacked" model proposed by Gerstoft [34]. In addition, Saeger et al. [35] modified and evaluated the 3-PJ model and showed that it could fit the measured atmospheric refractivity profile better. The 3-PJ model is formally a segmented function, including an evaporation layer segment and a mixed layer segment:

$$M(z)=M_0+\begin{cases}c_0\left(z-\delta\ln\left(\dfrac{z+0.00015}{0.00015}\right)\right), & z\le z_L\\ m_1 z-M_1, & z>z_L\end{cases} \quad (9)$$

where c_0 is defined as potential refractivity gradient (PRG). m_1 is mixed layer slope (MLS). z_L is evaporation layer height, $z_L=2\delta$. The three parameters c_0, m_1, and δ are the modeling parameters in the 3-PJ model. M_1 is used to ensure that the profile is continuous between the two layers, and is defined by other parameters (c_0 , m_1 , and δ). The uniqueness of the 3-PJ model is that it can make the shape of the *M*-profile more variable by adjusting the EDH, PRG, and MLS so that it can have a more accurate fit to measured atmospheric refractivity profile than the PJ model [14].

C. Markov Chain

To simulate the propagation of radio waves in non-uniform evaporation ducts, it is essential to calculate the *M*-profiles along the radio wave propagation path. The EDH parameters at different propagation distances can be calculated using the NPS model. Additionally, the non-uniform PRG and MLS parameters along the radio wave propagation path can be generated by the Markov chain simulation [34]. The non-uniform variations of PRG and MLS can be simulated as follows according to the Markov chain:

$$\mathbf{H}=[p_1,p_2,\cdots] \quad (10)$$

$$p_1=p_0 \quad (11)$$

$$p_{i+1}=p_i+\eta_i \quad (12)$$

$$\eta_i\sim N(0,\sigma_\eta^2) \quad (13)$$

where $\mathbf{H}$ is a Markov chain. p_i is the PRG or MLS parameter. p_0 is the PRG or MLS at the initial distance. It is a random variable that follows a Gaussian distribution, with a mean of zero and a variance of σ_η^2. σ_η^2 reflects the variation of the two parameters with the propagation distance.

D. Standard Parabolic Equation Algorithm

The standard parabolic equation (SPE) is a commonly used algorithm to describe the propagation characteristics of radio waves in atmospheric ducts [36]. It relies on the parabolic partial differential equation [37]. Furthermore, the SPE can be used to calculate radio wave propagation problems in irregular terrain and non-uniform atmospheric environments. In the Cartesian coordinate system, assuming that radio wave propagates along the horizontal direction, the SPE can be derived from the Helmholtz equation and has the form [38]:

$$\frac{\partial^2 u(x,z)}{\partial z^2}+2ik\frac{\partial u(x,z)}{\partial x}+k^2(n^2(x,z)-1)u(x,z)=0 \quad (14)$$

where k is the free-space wavenumber. x and z are the horizontal distance and the height. n is refraction index. u is a simplified field component function introduced to describe the amplitude variation of the electric field or magnetic field. The relation between field component and electric field or magnetic field is:

$$u(x,z)=\psi(x,z)e^{-ikx} \quad (15)$$

where ψ is the electric field or magnetic field. In addition, the SPE is mainly suitable for calculating the propagation problems of radio waves with propagation angles less than 15° [36]. Because the propagation angle of long-distance propagation is relatively small, the SPE has sufficient accuracy. This is consistent with the over-the-horizon propagation of radio waves in atmospheric ducts.

The commonly used method for solving SPE is the Split-Step Fourier Transform (SSFT) [39]. The SSFT allows for a larger step length and uses Fast Fourier Transform (FFT) without matrix operation, thus greatly speeding up the solution. Moreover, SSFT has different implementations depending on the lower boundary. For impedance boundary conditions the discrete mixed Fourier Transform (DMFT) is usually used to solve the SPE [38]. Kuttler et al. [40] analyzed forward, backward, and center differential DMFT and showed that backward differential DMFT has the best numerical stability. Therefore, this study employs the backward differential DMFT_SPE algorithm to study radio wave propagation in non-uniform evaporation ducts. The detailed solution processes for the DMFT_SPE algorithm can be found in [38].

E. LSTM Network and Transformer

1) LSTM Network: The LSTM network introduces a gating mechanism to effectively manage information flows [18], which consists of a forget gate, an input gate, and an output gate, as shown in Fig. 1. This gating mechanism allows the LSTM network to remember and forget information selectively at different moments, facilitating better processing of temporal relationships. In addition, memory cell in the LSTM block allows the network to selectively forget or remember information, thus effectively solving the problem of long-term dependence. The calculation processes of the three gates can be calculated as:

$$f_t=\sigma(W_i\cdot[H_{t-1},X_t]+b_f) \quad (16)$$

$$i_t=\sigma(W_i\cdot[H_{t-1},X_t]+b_i) \quad (17)$$

$$o_t=\sigma(W_o\cdot[H_{t-1},X_t]+b_o) \quad (18)$$

The update of memory cell can be expressed as:

$$C_t=f_t\odot C_{t-1}+i_t\odot tanh(W_c\cdot[H_{t-1},X_t]+b_c) \quad (19)$$

Finally, the output of the LSTM block is obtained:

$$H_t=o_t\odot\tanh(c_t) \quad (20)$$

where f_t , i_t, and o_t are forget gate, input gate, and output gate, respectively. C_t is memory cell. X_t and H_t are the input and final output. W is the weight and b is the bias (their subscripts are omitted for convenience). $\sigma(\cdot)$ and $\tanh(\cdot)$ represent the sigmoid and hyperbolic tangent functions.

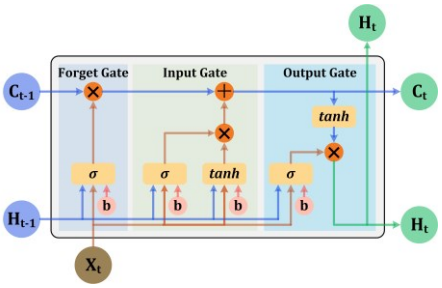

Fig. 1. LSTM block and its gating mechanism.

2) Transformer: The Transformer is a sequence-to-sequence model with an Encoder and a Decoder [25]. As shown in Fig. 2, the Encoder includes a multi-head self-attention module and a position-wise feed forward network (FFN). The self-attention is an important component, that enables the Transformer to calculate the importance of each position of the sequence. The self-attention maps each position in the input sequence into Query, Key, and Value vectors, and obtains the attention score of the position through dot product operation and weighted summation. To enhance the feature extraction ability, the Transformer uses multiple parallel self-attention. Therefore, multi-head self-attention allows the Transformer to learn different expressions of Query, Key, and Value vectors in each self-attention, and then combine the results of different self-attention to obtain a more comprehensive expression of features. The output of the multi-head self-attention in the Encoder is:

$$MultiHead(\mathbf{Q},\mathbf{K},\mathbf{V}) = \mathrm{Concat}(head_1,\ldots,head_h)W^O$$
$$\text{where } head_i = \mathrm{Softmax}\left(\frac{\mathbf{Q}W_i^{\mathbf{Q}}(\mathbf{K}W_i^{\mathbf{K}})^\top}{\sqrt{d_k}}\right)(\mathbf{V}W_i^{\mathbf{V}}) \quad (21)$$

where $head_i$ is self-attention. h is the number of heads of self-attention. $\mathbf{Q}$, $\mathbf{K}$, and $\mathbf{V}$ are the Query, Key, and Value vectors, respectively. $W^{\mathbf{Q}}$, $W^{\mathbf{K}}$, $W^{\mathbf{V}}$, and W^O are weights. d_k is the dimensional number of the Key. Softmax(·) represents a softmax activation function. Concat(·) represents the concatenation operation.

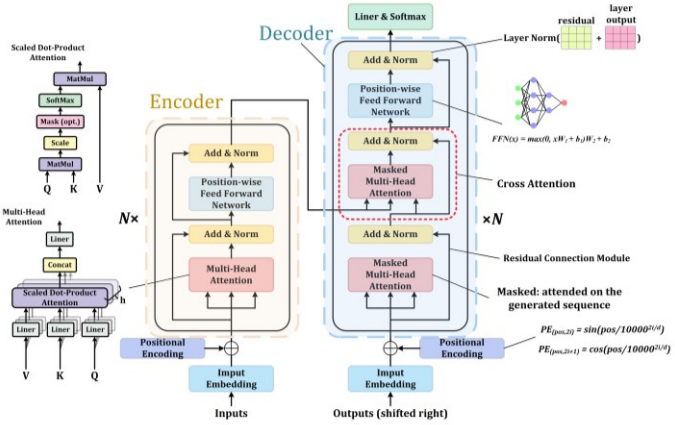

Fig. 2. Basic architecture of Transformer and its main components.

IV. Data

A. ERA5 Reanalysis Data

The ERA5 is the fifth generation of atmospheric reanalysis data [41]. It incorporates diverse global observations from weather stations, satellites, and other sources. Through data assimilation into a numerical weather prediction model, it produces a comprehensive and coherent representation of the atmospheric state. Therefore, ERA5 reanalysis data is widely used in the study of evaporation ducts [41]. In this study, the meteorological variables extracted from ERA5 include AT, AP, u-component of wind, v-component of wind, dewpoint temperature (DT), and SST. The reanalysis heights of extracted meteorological variables are shown in Table I.

TABLE I
REANALYSIS HEIGHTS OF METEOROLOGICAL VARIABLES

Meteorological variable	Reanalysis height	Unit
AP	0 m (surface)	hPa
SST	0 m (surface)	℃
AT	2 m	℃
DT	2 m	℃
U-component of wind	10 m	m/s
V-component of wind	10 m	m/s

In addition, this study selects the South China Sea (SCS) to study the propagation of radio waves. For this region, this study extracts the above six meteorological variables at 0:00 on May 1, 2023 (UTC). The regional distributions of these variables are shown in Fig. 3. It can be seen that each meteorological variable is non-uniform in different regions. This is because the environments in different regions are influenced by meteorology to different degrees. The non-uniformity of meteorological variables can also cause the non-uniformity of the evaporation duct.

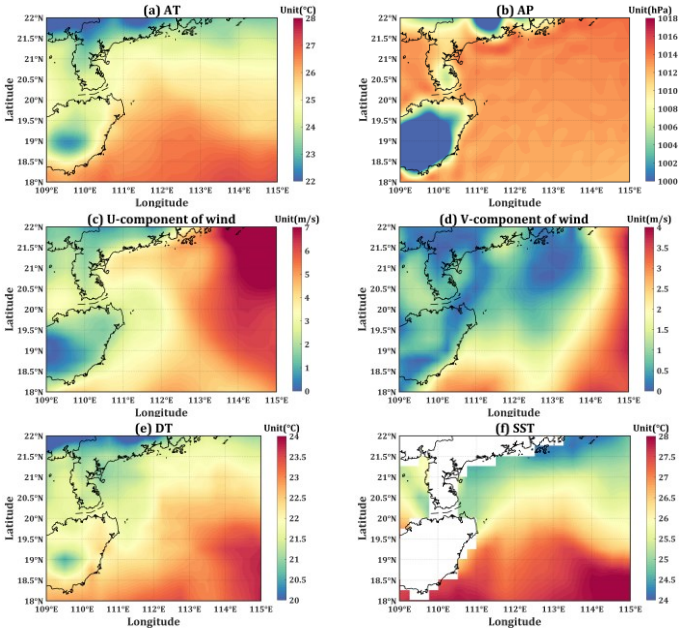

Fig. 3. Extracted (a) AT, (b) AP, (c) u-component of wind, (d) v-component of wind, (e) DT, and (f) SST variables from the ERA5 dataset.

Since the NPS model uses AT, AP, WS, RH, and SST to calculate the EDH, this study uses u-component of wind and v-component of wind to calculate the WS. Moreover, the DT and AT are used to calculate the RH using the Magnus-Tetens Approximation (MTA) equation [42], [43]. This MTA equation considers Magnus coefficients and can express the relation between DT, AT, and RH as:

$$RH = \exp\left(\frac{\beta \times D_p}{\lambda + D_p} - \frac{\beta \times T}{\lambda + T}\right) \times 100 \tag{22}$$

where D_p is DT. β =17.625 and λ =243.04℃ are revised Magnus coefficients [42]. According to (22) the conversion of AT and DT to RH can be realized.

B. Measured OHPL Data and EDH Data

The measured OHPL Data and EDH Data used in this study are provided by the China Research Institute of Radiowave Propagation (CRIRP), which are obtained from the Radio Wave Over-the-Horizon Propagation Measurement Experiment (RWOHPME) [44]. As shown in Fig. 4(a), the RWOHPME was conducted in the SCS, using a shipborne S-band radar installed on the "Qiongsha 3" ship.

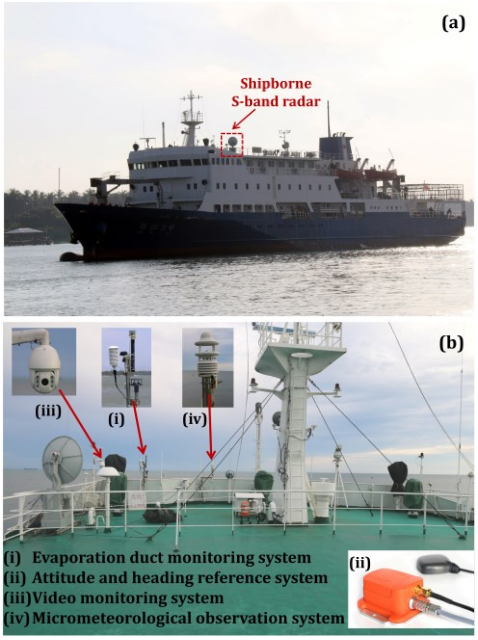

Fig. 4. Scene for conducting the RWOHPME: (a) "Qiongsha 3" ship and shipborne S-band radar, (b) equipment installed on the deck.

During the RWOHPME, the "Qiongsha 3" ship navigates from Wenchang City (19°33' N, 110°49' E) to Yongxing Island (16°84' N, 112°33' E), during which the shipborne S-band radar continuously transmits signals to a receiver located on the coast of Wenchang City. The receiver was equipped with an EMI signal receiver to continuously monitor and receive over-the-horizon signals. Simultaneously, a low-noise amplifier was installed at the front end of the receiver to enhance the signal-to-noise ratio. Therefore, the OHPL is collected during the navigation of the "Qiongsha 3" ship. According to the radar equation, the one-way OHPL of radio waves is calculated as [45]:

$$L = P_t + G_t + G_r + G_{LNA} - P_r - L_{r1} - L_{r2} \tag{23}$$

where P_t and P_r are the radar transmitting power and receiver receiving power. G_t and G_r are the transmitting gain and receiving gain. G_{LNA} is the low noise amplifier gain, L_{r1} and L_{r2} are the feedline losses of transmitter and receiver. The configurations of the above equipment parameters are shown in Table II.

TABLE II
EQUIPMENT PARAMETERS CONFIGURATIONS

Parameter	Value	Unit
P_t	41.8	dBm
G_t	28	dBi
G_r	16	dBi
G_{LNA}	22.25	dBi
L_{r1} , L_{r2}	2	dB

Three sets of over-the-horizon propagation signals were measured in the RWOHPME. According to (23) and equipment parameters, this study calculates the OHPLs of these three sets of over-the-horizon signals. The measured OHPLs for the three sets are shown in Fig. 5.

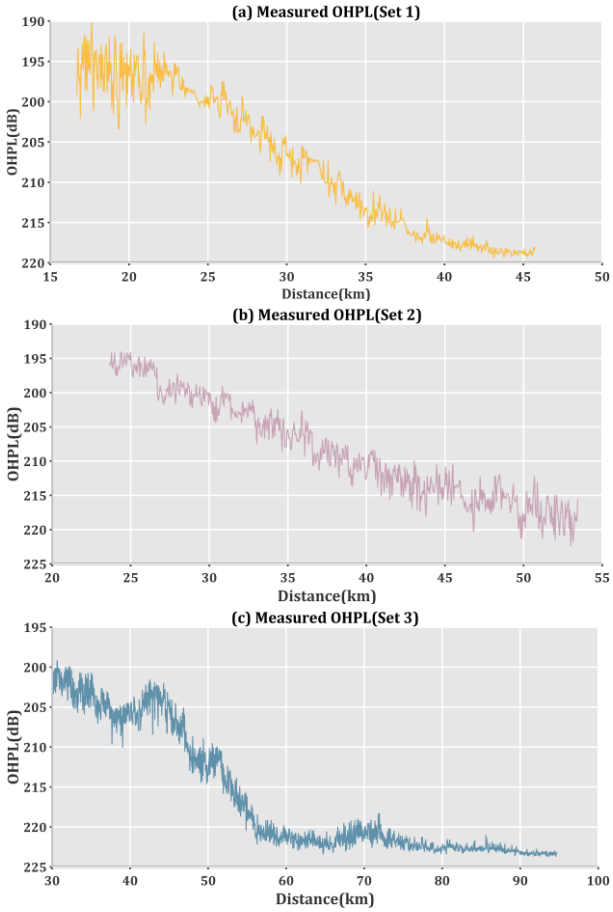

Fig. 5. Measured OHPLs of (a) *Set 1*, (b) *Set 2*, and (c) *Set 3*.

In addition, an evaporation duct monitoring system (EDMS) is installed on the "Qiongsha 3" ship to measure EDH on the "Qiongsha 3" ship route. The EDMS and other auxiliary systems are shown in Fig. 4(b). During the RWOHPME, the S-band radar and the EDMS worked simultaneously, and the measured EDH were used to support the analysis of the radio waves over-the-horizon propagation characteristics. Three sets of EDH data simultaneously measured are shown in Fig. 6.

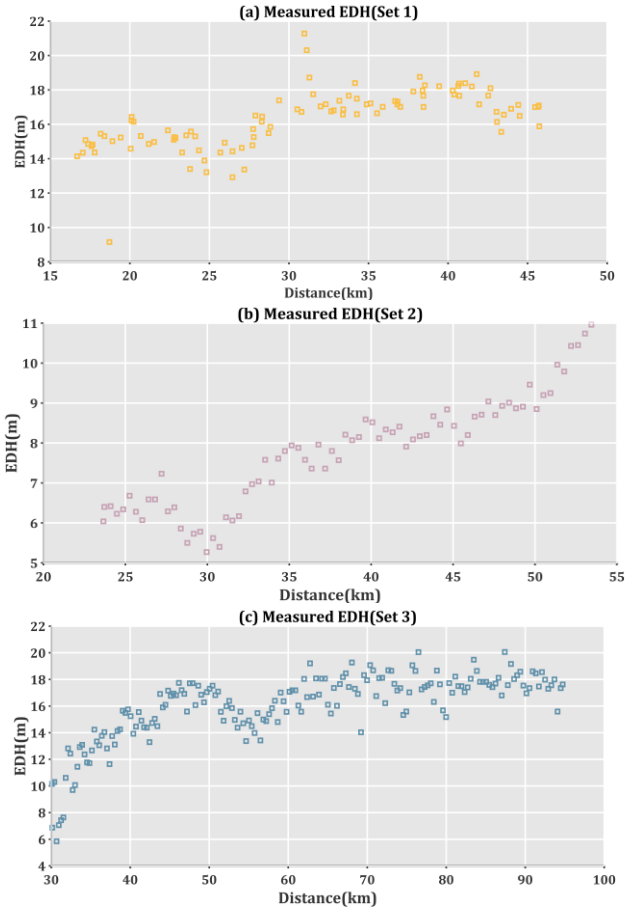

Fig. 6. Simultaneously measured EDH of (a) *Set 1*, (b) *Set 2*, and (c) *Set 3*.

V. Establishment of the IPILT-OHPL Prediction Model

A. The Overall Establishment Process of the IPILT-OHPL Model

This study purposely establishes the IPILT-OHPL prediction model to accurately predict the OHPL by incorporating EDH as an environmental prior information to the combined LSTM-Transformer. The overall establishment process of the IPILT-OHPL model is shown in Fig. 7. This study extracts the meteorological variables needed to calculate EDH from the ERA5 dataset. Additionally, this study uses the 3-PJ model to calculate the non-uniform *M*-profiles. Subsequently, the *M*-profiles at different propagation distances are calculated. These non-uniform *M*-profiles are then integrated into the SPE algorithm to simulate the OHPL. Subsequently, a specific dataset is constructed using measured and simulated OHPLs and divided into training and test sets. The training set is used to train the LSTM-Transformer, completing the training to obtain the LT-OHPL model. This study then uses the test set to evaluate the performance of LT-OHPL. The detailed establishment process is described in the following sections.

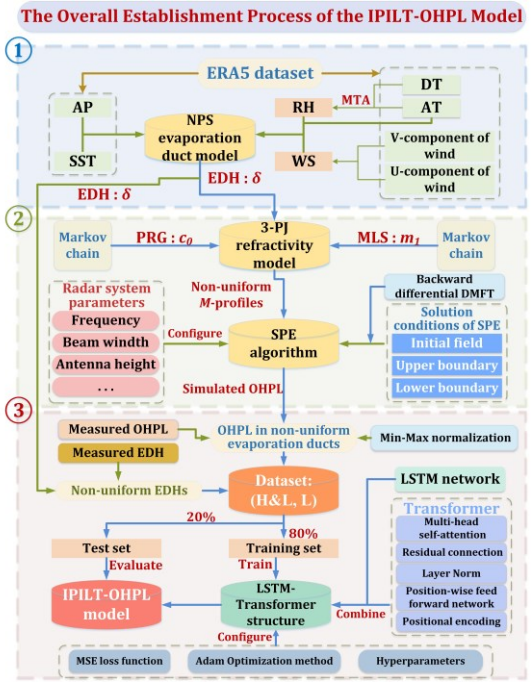

Fig. 7. Overall establishment process of the IPILT-OHPL model.

B. Calculating the Non-Uniform Evaporation Ducts

To simulate the OHPL in non-uniform evaporation ducts, the *M*-profiles of non-uniform evaporation ducts are crucial. Therefore, this study uses specific meteorological variables to calculate the *M*-profiles that vary with distance. This study first extracts six meteorological variables from the ERA5 dataset. This study then calculates WS based on the components of WS and calculates RH using DT and AT. The five meteorological variables are linearly interpolated and then are input into the NPS model to obtain the regional distribution of the EDHs. The calculated non-uniform EDHs in the SCS are shown in Fig. 8.

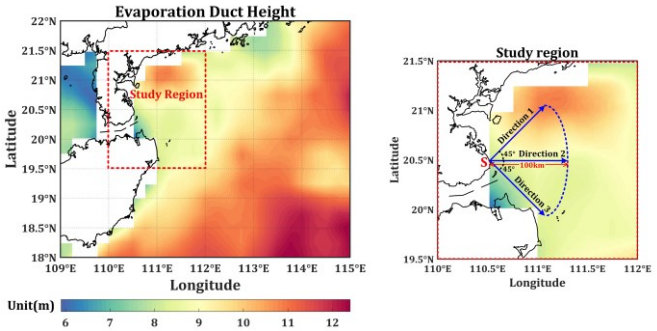

Fig. 8. Non-uniform EDH distribution and study region.

Furthermore, to simulate different OHPLs for verifying the generalization ability of the IPILT-OHPL model, a specific study region is selected for this study. This study takes "S" as the transmitter source of the radio waves and simulate the

OHPL for three different directions in this region, as shown in Fig. 8. The EDHs in the three directions have certain fluctuations with the propagation distance, reflecting different degrees of regional non-uniformity.

Then the calculated non-uniform EDHs in three directions are input into the 3-PJ model to calculate the *M*-profiles varying with the propagation distance. In addition, the 3-PJ model is determined by EDH, PRG, and MLS parameters. The PRG and MLS parameters varying with the propagation distance can be simulated by the Markov chain. Similarly, this study uses the Markov chain to simulate three sets of non-uniform PRG and MLS parameters, respectively. The Markov chain simulation results for two parameters are shown in Fig. 9. Finally, the non-uniform EDH, PRG, and MLS parameters in each direction are then input into the 3-PJ model to calculate non-uniform *M*-profiles in that direction.

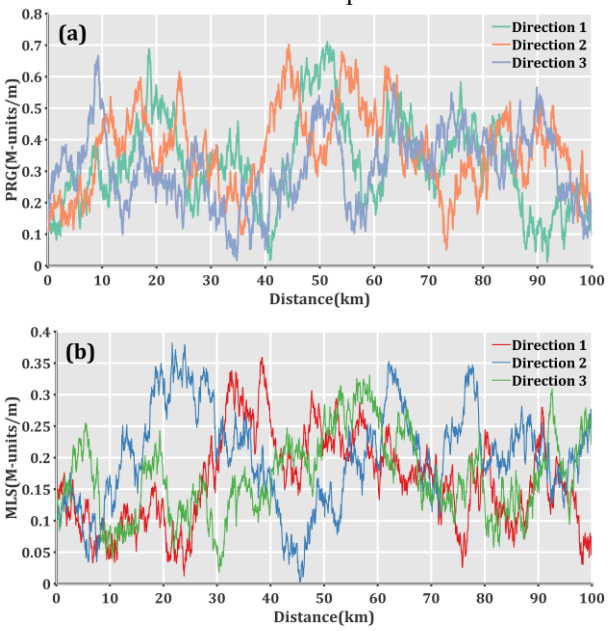

Fig. 9. Markov chain simulation results of non-uniform (a) PGR and (b) MLS parameters in three directions.

C. Simulating the OHPL in Non-uniform Evaporation Ducts

The OHPL at different propagation distances can be calculated as:

$$L = -20\log|u(x,z)| + 20\log(4\pi) + 10\log x - 30\log\lambda \quad (24)$$

where λ is the wavelength. The field components $u(x,z)$ at different distances can be derived by conducting stepwise calculations on (14). When using the backward differential DMFT_SPE algorithm to conduct stepwise calculations of the field components, this study adjusts the refractive environment at each propagation distance using the calculated non-uniform *M*-profiles. This method allows for obtaining the field components at different distances in non-uniform evaporation ducts. Ultimately, the OHPL in non-uniform evaporation ducts can be calculated by inputting field components at different propagation distances into (24). Fig. 10 shows the spatial distributions of the simulated OHPL.

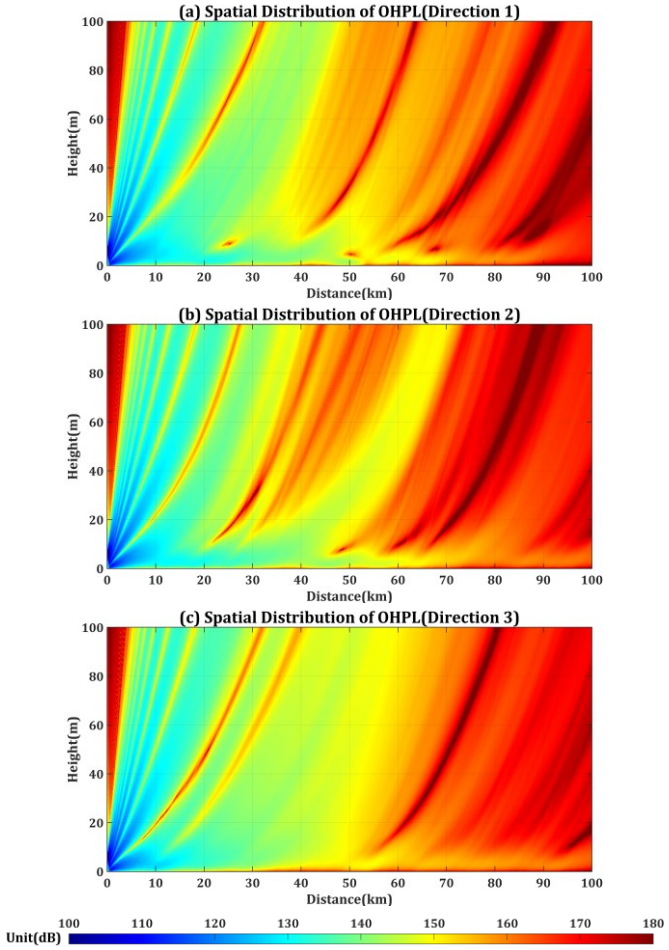

Fig. 10. Spatial distributions of the simulated OHPLs in (a) *Direction 1*, (b) *Direction 2*, and (c) *Direction 3*.

It can be observed that there are significant differences in spatial distributions of simulated OHPL in different propagation directions. This is because the non-uniform evaporation duct environments in different propagation directions are different. Under the influence of non-uniform evaporation ducts, the trapping layers at different distances have different trapping degrees for radio waves. This significantly influences the variation of OHPL distribution with propagation distance and height. The radar system parameter configurations used for simulating the OHPL are shown in III.

TABLE III
RADAR SYSTEM PARAMETERS CONFIGURATIONS

Parameter	Value	Unit
Frequency	10	GHz
Beam width	0.7	°
Antenna tilt angle	0	°
Antenna height	6	m
Antenna type	Gaussian antenna	-
Polarization	Vertical	-

In three spatial distributions of simulated OHPL, this study selects the OHPL at a height of 13m above the marine surface. The selection of this height considers the operational height of RES in the marine environment, as it is the typical height

used for RES on ship [46]. The simulated OHPLs used in this study are shown in Fig. 11.

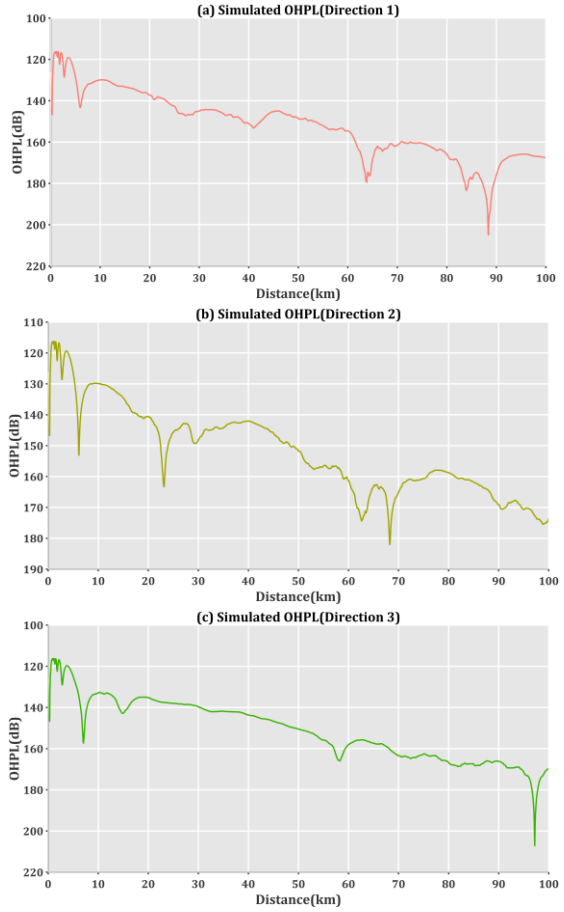

Fig. 11. Simulated OHPLs in (a) *Direction 1*, (b) *Direction 2*, and (c) *Direction 3* in non-uniform evaporation ducts.

D. Training the LSTM-Transforermer Structure

1) Combining LSTM Network and Transformer: This study constructs an LSTM-Transformer structure that combines the LSTM network and Transformer specifically for OHPL prediction. As the Encoder block excels in processing sequence features, employing only the Encoder suffices for OHPL prediction. Using only the Encoder simplifies the LSTM-Transformer, mitigating overfitting risk and thus enhancing generalization and calculation efficiency.

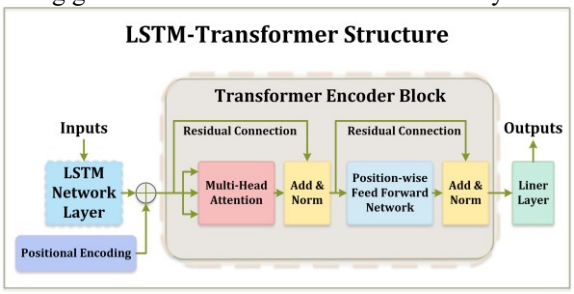

Fig. 12. LSTM-Transformer structure and its components.

As shown in Fig. 12, the LSTM-Transformer mainly consists of four components: an LSTM network layer, a position encoding layer, a Transformer Encoder block, and a liner layer. The LSTM network's output serves as the input to the Transformer, which then uses multi-head self-attention for additional local features extraction. Moreover, the position encoding layer uses sine and cosine functions to encode the LSTM network's output, and the encoded feature is input into the multi-head self-attention layers for parallel feature extraction. Finally, the feature from the multi-head self-attention undergoes linear transformation via a linear layer to output the predicted results.

2) Constructing the Dataset: The OHPL is directly correlated with the EDH in non-uniform evaporation ducts. Both EDH and OHPL need to be considered as input feature variables. Therefore, the LSTM-Transformer can more fully understand the influences of non-uniform evaporation ducts on OHPL, thereby enhancing the accuracy and robustness of prediction. According to the input and output of the IPILT-OHPL model, this study constructs a specific dataset $(\mathbf{H}\,\&\,\mathbf{L},\mathbf{L})$, where the input variables $\mathbf{H}\,\&\,\mathbf{L}$ can be expressed as:

$$\mathbf{H}\,\&\,\mathbf{L}=\left\{(H,L)_1,(H,L)_2,...,(H,L)_{\tilde{T}}\right\} \tag{25}$$

where H is the EDH at different moments. Given that the OHPL in the future serves as the IPILT-OHPL model's output, OHPL is designated as the output variable of the LSTM-Transformer, which can be expressed as:

$$\mathbf{L}=\left\{L_1,L_2,...,L_{\tilde{T}}\right\} \tag{26}$$

Since this study uses six sets of OHPLs and their corresponding EDHs, six different datasets $(\mathbf{H}\,\&\,\mathbf{L},\mathbf{L})$ are constructed. In addition, the first 80% of each $(\mathbf{H}\,\&\,\mathbf{L},\mathbf{L})$ is divided into training set for training the LSTM-Transformer. The remaining 20% is used as a test set to evaluate the prediction performance of the IPILT-OHPL model. Furthermore, to enhance the convergence velocity and prediction accuracy, the OHPL sequence is processed using the Min-Max normalization method before training.

3) Configuring Loss Function and Optimization Method: This study selects the MSE as the loss function, which is calculated as (27). In the LSTM-Transformer training, the loss function measures its performance by calculating the difference between predicted results and the corresponding OHPL in the training set. Through iterating loss function, the LSTM-Transformer improves its performance, aiming for strong generalization to unseen data.

$$Loss=\frac{\sum_{i=1}^{H}\left(L_i^{pred}-L_i\right)^2}{H} \tag{27}$$

where H is the size of the training set. L_i^{pred} and L_i are the predicted OHPL and corresponding label. Furthermore, this study uses the Adaptive Moment Estimation optimization method to modify the weights of LSTM-Transformer, aiming to minimize the loss function until achieving a stable state.

4) Configuring Hyperparameters: By performing prediction experiments for the LSTM-Transformer on the training set, this study finally obtains the OHPL prediction model, i.e., the IPILT-OHPL model. Since the

hyperparameters have a crucial influence on the performance of the trained model, it is important to select and debug these hyperparameters. This study involves configuring hyperparameters for the main components in the LSTM-Transformer and training-related hyperparameters, such as batch size, learning rate, and epochs. In the training process, this study gets the feedback on the training results through many prediction experiments, and gradually optimizes the selection of parameters based on certain empirical knowledge. The detailed configurations of the hyperparameters are shown in Table IV.

TABLE IV
DETAILED HYPERPARAMETERS CONFIGURATIONS

Hyperparameter		Value
LSTM-Transformer structure component	LSTM network layer (M=1)	Input size (d=32) Hidden layer neurons (n=64) Dropout (p=0.2) Output (d_{out}=64)
	Positional encoding	Encoding (d_{model}=64)
	Transformer Encoder block (N=1)	Multi-head self-attention (h=2) Add, Layer Norm, Dropout (p=0.1) Position-wise FFN (d_{inner}=128), RELU Add, Layer Norm, Dropout (p=0.1)
	Linear layer (L=1)	Output (d_{out}=1)
Training-related hyperparameter		Batch size ($batch\_size$=32) Epochs (i=150) Learning rate (l=0.005)

VI. PREDICTED RESULTS AND EVALUATIONS

In this study, the input variables in the test set are input into the established IPILT-OHPL model, and then the predicted results of the IPILT-OHPL model are compared with the output variable in the test set to evaluate the performance of the IPILT-OHPL model. In addition, to show the superiority of the IPILT-OHPL model, this study uses the LSTM network, Transformer, LSTM-Attention, RNN-Transformer, and LSTM-Transformer to additionally establish OHPL prediction models for comparison with the IPILT-OHPL model. There is no EDH in the input variables of the above comparison models, only OHPL. To further test the performance of the IPILT-OHPL model in different application scenarios, this study evaluates the model from two different aspects: one-step prediction and multiple-step prediction.

A. Evaluating the IPILT-OHPL Model Performance in One-Step Prediction

Firstly, this study evaluates the performance of the IPILT-OHPL model in one-step OHPL prediction. In this evaluation, this study uses the input variables from the former 24 steps to predict the subsequent OHPL. The subsequent predicted step length is set to 1. This study first visualizes the predicted results from all models on the test set to more intuitively observe predicted results and compare performance. As shown in Fig.13, all prediction models show different predicted results across different OHPL sequences, mainly influenced by inherent OHPL characteristics and different model structures.

Due to the non-uniform evaporation ducts, the simulated OHPLs in the test set show significant fluctuations in Fig. 13(a) and (c), which have great influences on predicted results. Both the LSTM and LSTM-Attention are difficult to fit the OHPL effectively due to their limited feature extraction ability. In comparison, the Transformer, RNN-Transformer, and LSTM-Transformer exhibit better OHPL fitting due to their superior feature extraction abilities. This is because Transformer, RNN-Transformer, and LSTM-Transformer use multi-head self-attention to extract local features in the OHPL. In addition, the OHPL does not fluctuate greatly in Fig. 13(b), therefore all the prediction models have good predicted results, and the differences between them are not obvious.

Compared with the simulated OHPLs, the measured OHPLs show more local fluctuations in Fig. 13(d)-(e). The LSTM and LSTM-Attention can only approximately fit the overall trend of the OHPL, but they are difficult to extract local fluctuation features effectively. Especially when the local fluctuations of the OHPL are intense, the predicted results of these two models deviate more from the OHPL. The Transformer, RNN-Transformer, and LSTM-Transformer models exhibit better fit on local features. However, in the presence of more local fluctuations, the Transformer cannot fit the overall trend of the OHPL well.

Notably, the IPILT-OHPL model shows better predicted results on all test sets. It not only effectively fits the overall trend of the OHPLs, but also accurately extracts the local features of the OHPLs. This shows that the IPILT-OHPL model has strong generalization ability and feature extraction ability in predicting OHPL. The superior performance of the IPILT-OHPL model is not only due to the strong feature extraction ability of the LSTM-Transformer structure but also because it incorporates the EDH as the environmental prior information of the model. By incorporating these EDHs at different distances into the input of the model, the model can more accurately understand and predict the OHPL in complex non-uniform evaporation ducts.

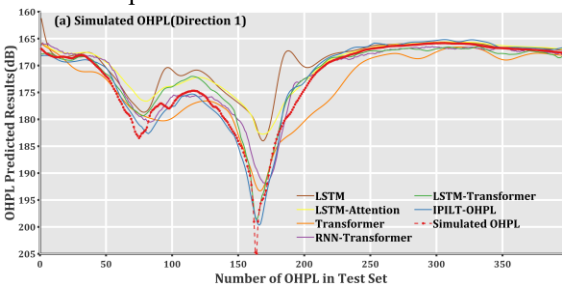

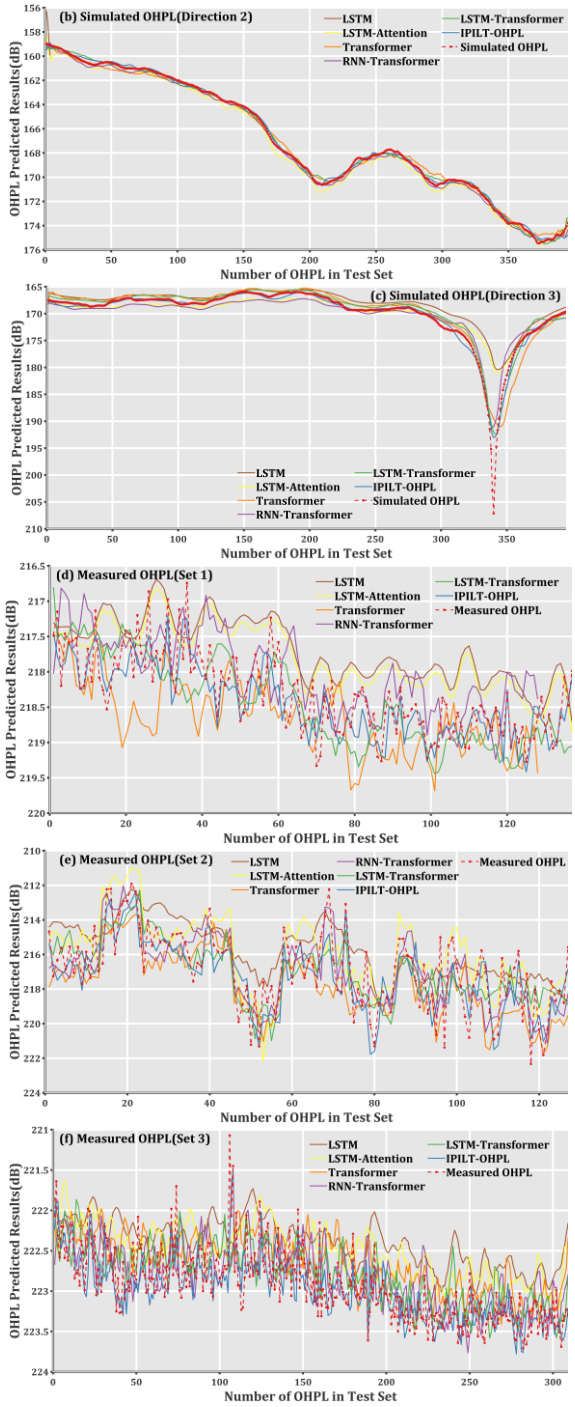

Fig. 13. Predicted results of the simulated OHPLs in (a) *Direction 1*, (b) *Direction 2*, and (c) *Direction 3* and the measured OHPLs of (d) *Set 1*, (e) *Set 2*, and (f) *Set 3*.

To quantitatively evaluate the prediction errors of different models, this study calculates the evaluation indicators for all predicted results on the test set. The evaluation indicators include root mean square error (RMSE), mean absolute error (MAE), mean absolute percentage error (MAPE), and coefficient of determination (R2), which can be calculated by the following (28)-(31), respectively. Where RMSE, MAE, and MAPE are commonly used evaluation indicators to measure the difference between the predicted results and corresponding labels [47]. When their values are smaller, it means that the model's predicted results are more accurate and the model's performance is better. In addition, R2 is used to describe the degree of fitting between the model's predicted results and corresponding labels. The larger the R2, the better the prediction performance of the model.

$$RMSE = \sqrt{\frac{\sum_{j=1}^{N}\left(L_j^{pred} - L_j\right)^2}{N}} \tag{28}$$

$$MAE = \frac{\sum_{j=1}^{N}\left|L_j^{pred} - L_j\right|}{N} \tag{29}$$

$$MAPE = \frac{100\%}{N}\sum_{j=1}^{N}\left|\frac{L_j^{pred} - L_j}{L_j}\right| \tag{30}$$

$$R2 = 1 - \frac{\sum_{j=1}^{N}(L_j - L_j^{pred})^2}{\sum_{j=1}^{N}(L_j - \bar{L})^2} \tag{31}$$

where N is the size of the test set. $\bar{L}$ is the mean value of the OHPL in the test set.

This study then compares the prediction performance between the models according to the evaluation indicators. As shown in Fig. 14, the IPILT-OHPL model consistently maintains the best evaluation indicators in all test sets compared to the other models. This shows that the IPILT-OHPL model always shows superior prediction performance in all OHPL test sets. This model not only has good prediction performance but also has strong generalization ability. Followed by the LSTM-Transformer, its evaluation indicators are second only to the IPILT-OHPL model. This indicates that the prediction performance of the LSTM-Transformer is second only to the IPILT-OHPL model. In comparison, the LSTM has the worst evaluation indicators in most of the test sets (except for the R2 for the measured OHPL of *Set 1*), indicating that its prediction performance is the worst among all models. In addition, all models show worse RMSE, MAE, and MAPE in predicting the simulated OHPL in *Direction 1*, but the IPILT-OHPL model still outperforms the other models in these indicators. Meanwhile, these indicators of the IPILT-OHPL model are improved by 71.376%, 64.571%, and 63.648%, respectively, compared to the LSTM. Compared with the LSTM-Transformer, these indicators of the IPILT-OHPL model are improved by 21.542%, 21.643%, and 21.836%, respectively.

Because there are many local fluctuations in the measured OHPLs, most of the models cannot accurately fit the overall trend of measured OHPLs. Most models show worse R2 in predicting the measured OHPLs, especially showing the lowest R2 when predicting the measured OHPL of *Set 3*. By using EDH as the prior information, the IPILT-OHPL model can cognize the influences of the environment on OHPL more comprehensively, and its predicted results better fit the overall trend of the OHPL. Therefore, the R2 of the IPILT-OHPL model is still higher than that of other models. The R2 of the IPILT-OHPL model is 0.310 and 0.213 higher than that of the LSTM and LSTM-Transformer respectively, in

predicting the OHPL of *Set 3*. In addition, all models have better evaluation indicators in predicting the simulated OHPL in *Direction 2*. Meanwhile, the RMSE, MAE, MAPE, and R2 of the IPILT-OHPL model can reach 0.204, 0.158, 0.094, and 0.999, respectively. It still has much higher RMSE, MAE, and MAPE than other models. Compared to the LSTM, these improvements are 50.244%, 54.467%, and 54.808% in the RMSE, MAE, and MAPE respectively. Furthermore, compared to the LSTM-Transformer, there are improvements of 9.735%, 9.714%, and 9.615%, respectively.

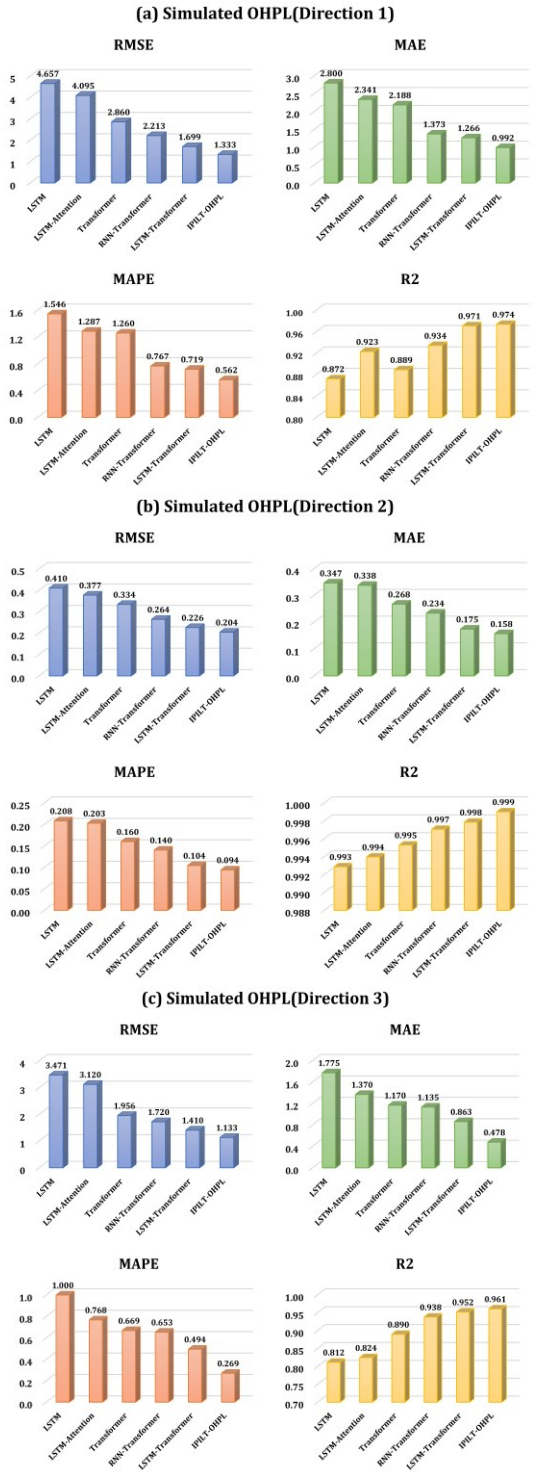

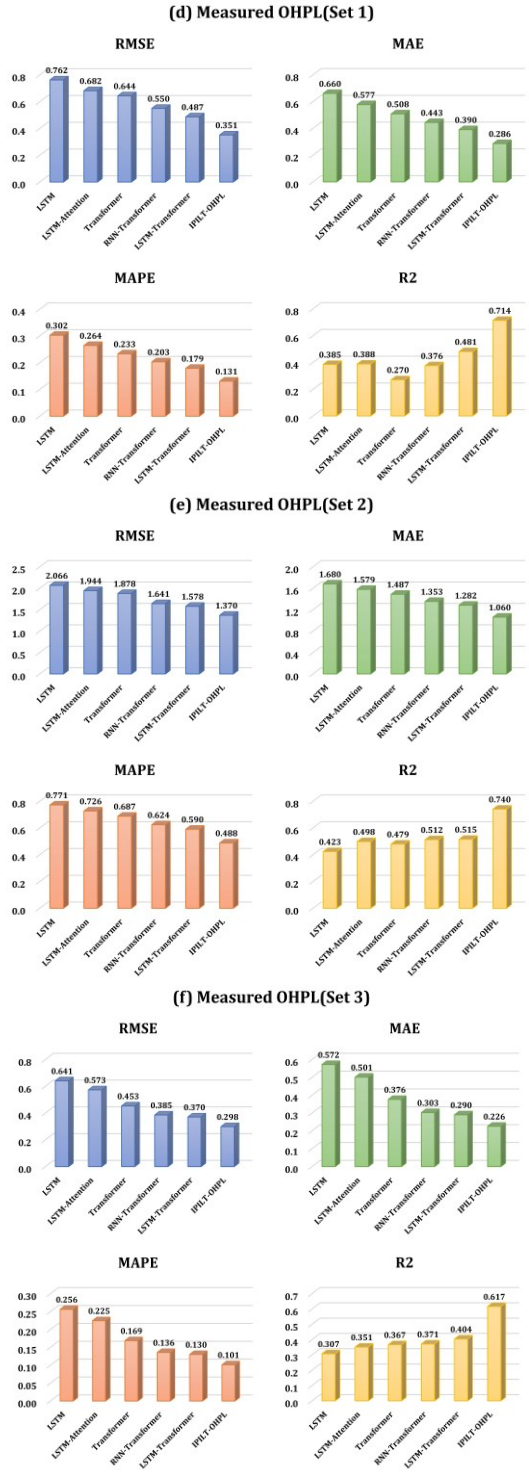

Fig. 14. Evaluation indicators of the simulated OHPLs in (a) *Direction 1*, (b) *Direction 2*, and (c) *Direction 3* and the measured OHPLs of (d) *Set 1*, (e) *Set 2*, and (f) *Set 3* for one-step prediction.

B. Evaluating the IPILT-OHPL Model Performance in Multiple-Step Prediction

To evaluate the multiple-step prediction performance of the IPILT-OHPL prediction model, this study further establishes the IPILT-OHPL model and other comparison models with predicted step lengths of 2, 4, 8, and 16. This

study calculates RMSE, MAE, MAPE, and R2 for all prediction models under different predicted step lengths based on the test set.

The evaluation indicators under different predicted step lengths are shown in Fig. 15. The evaluation indicators of all the models are getting worse as the predicted step length increases gradually. This shows that the prediction performance of all models is decreasing. When the predicted step length is 16, the prediction performance of all models is the worst. In addition, the IPILT-OHPL model consistently maintains the best evaluation indicators in all models as the predicted step increases. This shows that the IPILT-OHPL model has superior prediction performance even under larger steps. The IPILT-OHPL model also has better predicted results when the predicted step length is 16.

Similar to the predicted step length of 1, when the predicted step length is 16, all models also have the highest RMSE, MAE, and MAPE in predicting the OHPL in *Direction 1*. In addition, the RMSE, MAE, and MAPE of the IPILT-OHPL model are improved by 46.030%, 54.321%, and 41.927%, respectively, compared to the LSTM. Compared with the LSTM-Transformer, the three evaluation indicators of the IPILT-OHPL model are improved by 13.892%, 15.233%, and 21.020%, respectively.

Moreover, most models show the lowest R2 in predicting the measured OHPL of *Set 3* when the predicted step length is 16. The R2 of the IPILT-OHPL model is still higher than that of other models, which is 0.297 and 0.211 higher than that of LSTM and LSTM-Transformer, respectively. In predicting the Simulated OHPL of *Direction 2*, all models also have better evaluation indicators under the predicted step length of 16. Meanwhile, the evaluation indicators of the IPILT-OHPL model are still superior to other models. The RMSE, MAE, MAPE, and R2 of the IPILT-OHPL model are 0.487, 0.385, 0.237, and 0.990, respectively. In addition, the IPILT-OHPL model's RMSE, MAE, and MAPE improved by 36.999%, 46.379%, and 45.012% respectively compared to the LSTM, and improved by 14.860%, 16.847%, and 15.658% respectively compared to the LSTM-Transformer. Furthermore, the R2 of the IPILT-OHPL model is 0.013 and 0.004 higher than that of LSTM and LSTM-Transformer, respectively.

This study evaluates the prediction performance of the IPILT-OHPL model by calculating the evaluation indicators based on the test set in different application scenarios. Comprehensively, these evaluation indicators highlight the superior prediction performance of the IPILT-OHPL model. Its prediction performance is significantly better than that of other models. The IPILT-OHPL model not only has high accuracy but also shows strong generalization ability, which effectively processes the temporal relationships of the OHPL. The superior performance of the IPILT-OHPL model is not only due to the strong feature extraction ability of the LSTM-Transformer structure, but the model also uses EDH as prior information, thus enhancing its wide applicability.

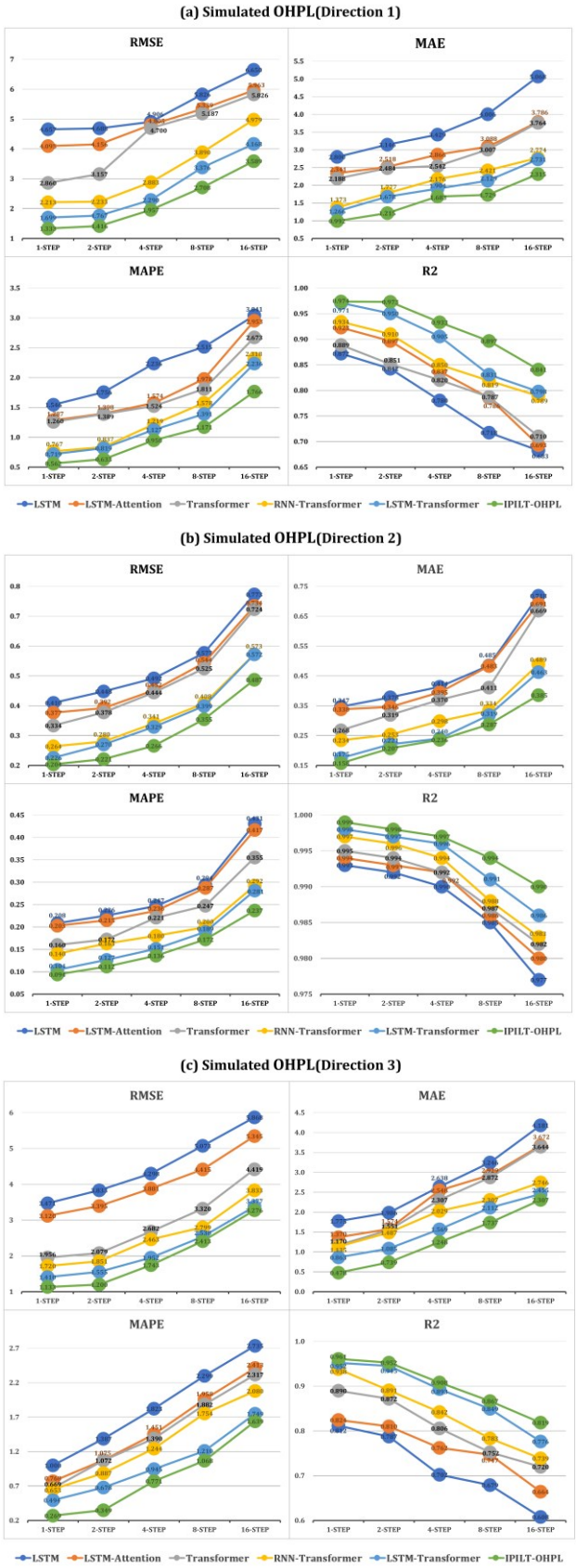

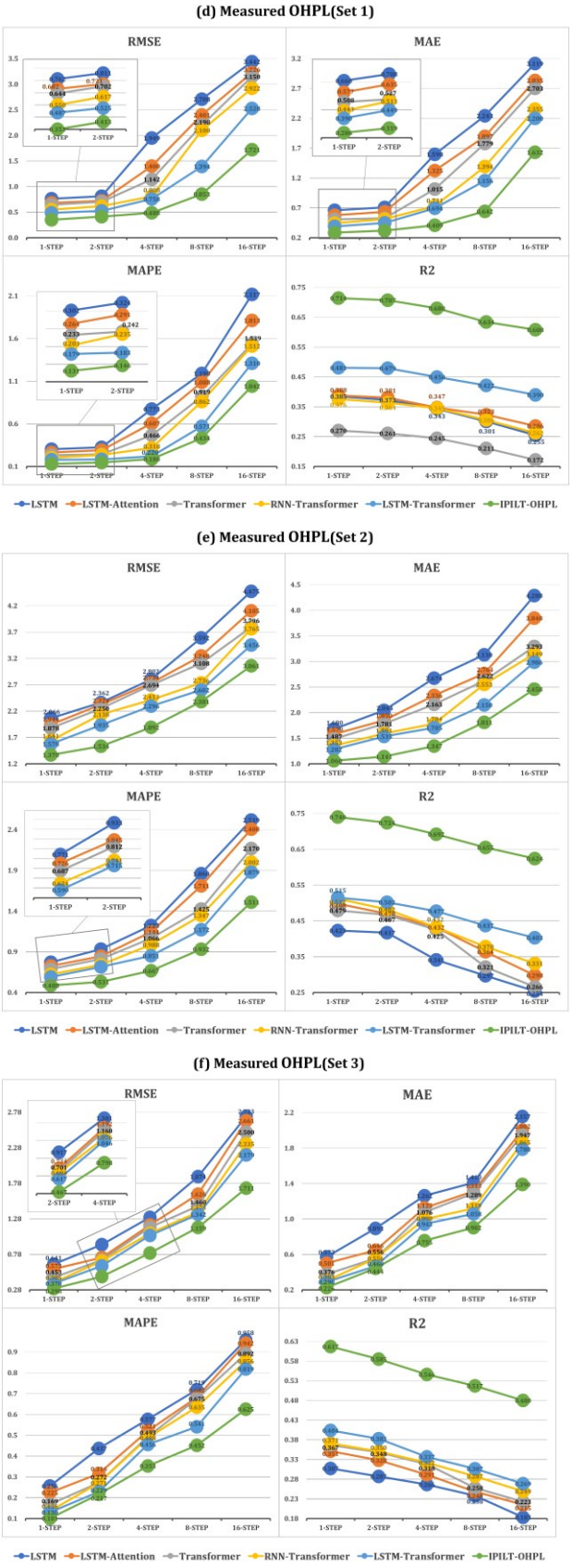

Fig. 15. Evaluation indicators of the simulated OHPLs in (a) *Direction 1*, (b) *Direction 2*, and (c) *Direction 3* and the measured OHPLs of (d) *Set 1*, (e) *Set 2*, and (f) *Set 3* for multiple-step prediction.

VII. Conclusion

To accurately predict the OHPL in marine non-uniform evaporation ducts, this study establishes the IPILT-OHPL model by incorporating EDH as an environmental prior information into the LSTM-Transformer structure. Because the radio waves are influenced by the non-uniform evaporation ducts, their OHPL will show local fluctuations at certain propagation distances. This study combines the LSTM network and Transformer and uses the combined LSTM-Transformer structure to enhance the LSTM network's ability for extracting OHPL features. Combining these two networks, the IPILT-OHPL model can capture different dependencies and local features more comprehensively when processing OHPL, thereby enhancing the prediction performance and generalization ability of the model. In addition, by incorporating EDH as prior information into the LSTM-Transformer structure, the model can better cognize the influences of non-uniform evaporation ducts on OHPL, thereby enhancing the prediction accuracy. This study comprehensively evaluates the IPILT-OHPL model performance. The evaluation results show the superior performance of the IPILT-OHPL model. It outperforms other prediction models in both one-step prediction and multiple-step prediction. Meanwhile, the IPILT-OHPL model has a strong generalization ability, which has better predicted results for different OHPLs. Therefore, the proposed IPILT-OHPL model has a more comprehensive performance in the field of OHPL prediction, which provides an effective method for predicting the OHPL in non-uniform evaporation ducts.

References

[1] S.-W. Wang, K.-D. Yang, Y. Shi, F. Yang, and H. Zhang, "Observed Over-the-Horizon Propagation Characteristics and Evaporation Duct Inversion During the Entire Process of Tropical Cyclone Mulan (202207)," *IEEE Trans. Antennas Propagat.*, vol. 71, no. 6, pp. 5322–5334, Jun. 2023.

[2] J. D. Turton, D. A. Bennetts and S. F. G. FARMER, "An introduction to radio ducting," *Meteorol. Mag.*, vol. 117, pp. 245–254, Jan. 1988.

[3] H. V. Hitney, J. H. Richter, R. A. Pappert, K. D. Anderson, and G. B. Baumgartner, "Tropospheric radio propagation assessment," *Proc. IEEE*, vol. 73, no. 2, pp. 265–283, Feb. 1985.

[4] Z.-H. Fu, F. Du, X.-W. Zhao, S.-Y. Geng, Y. Zhang, and P. Qin, "A Joint-Neural-Network-Based Channel Prediction for Millimeter-Wave Mobile Communications," *IEEE Antennas Wirel. Propag. Lett.*, vol. 22, no. 5, pp. 1064–1068, May. 2023.

[5] K. D. Anderson, "Radar measurements at 16.5 GHz in the oceanic evaporation duct," *IEEE Trans. Antennas Propag.*, vol. 37, no. 1, pp. 100–106, Jan. 1989.

[6] W.-J. Zhou, M.-W. Shen, Y. Zhang, D. Wu, and D.-Y. Zhu, "Offshore surface evaporation duct joint inversion algorithm using measured dual-frequency sea clutter," *IEEE J. Sel. Top. Appl. Earth Observ. Remote Sens.*, vol. 15, pp. 6382–6390, Aug. 2022.

[7] C. Yang, Y.-F. Shi, J. Wang, and F. Feng, "Regional spatiotemporal statistical database of evaporation ducts over the South China Sea for future long-range radio application," *IEEE J. Sel. Top. Appl. Earth Observ. Remote Sens.*, vol. 15, pp. 6432–6444, Aug. 2022.

[8] Q.-X. Liao, Y.-B. Mai, Z. Sheng, Y.-H. Wang, Q.-J. Ni, and S.-D. Zhou, "The Comparison of Long Short-Term Memory Neural Network and Deep Forest for the Evaporation Duct Height

Prediction," *IEEE Trans. Antennas Propagat.*, vol. 71, no. 5, pp. 4444–4450, May. 2023.

[9] A. Barrios, "Parabolic equation modeling in horizontally inhomogeneous environments," *IEEE Trans. Antennas Propag.*, vol. 40, no. 7, pp. 791–797, Jul. 1992.

[10] G. L. Geernaert, "On the evaporation duct for inhomogeneous conditions in coastal regions," *J. Appl. Meteorol. Climatol.*, vol. 46, pp. 538–543, Apr. 2007.

[11] S.-W. Wang, K.-D. Yang, Y. Shi, F. Yang, H. Zhang, and Y.-L. Ma, "Prediction of Over-the-Horizon Electromagnetic Wave Propagation in Evaporation Ducts based on the Gated Recurrent Unit Network Model," *IEEE Trans. Antennas Propagat.*, vol. 71, no. 4, pp. 3485–3496, Feb. 2023.

[12] Y. Shi, K.-D. Yang, Y.-X. Yang, and Y.-L. Ma, "Experimental verification of effect of horizontal inhomogeneity of evaporation duct on electromagnetic wave propagation," *Chin. Phys. B*, vol. 24, no. 4, pp. 197–205, Mar. 2015.

[13] D. P. Alappattu, Q. Wang, R. T. Yamaguchi, T. Haack, M. Ulate, H. J. Fernando, and P. Frederickson, "Electromagnetic ducting in the near-shore marine environment: results from the CASPER-east field experiment," *J. Geophys. Res. Atmos.*, vol. 127, no. 22, pp. 1–13, Oct. 2022.

[14] S. E. Penton and E. E. Hackett, "Rough ocean surface effects on evaporative duct atmospheric refractivity inversions using genetic algorithms," *Radio Sci.*, vol. 53, pp. 804–819, Jun. 2018.

[15] V. A. Permyakov, M. S. Mikhailov and E. S. Malevich, "Analysis of propagation of electromagnetic waves in difficult conditions by the parabolic equation method," *IEEE Trans. Antennas Propag.*, vol. 67, no. 4, pp. 2167–2175, Mar. 2019.

[16] H.-Z. Zhang, T. Zhou, T.-H. Xu, Y.-Z. Wang, and H.-L. Hu, "FNN-based prediction of wireless channel with atmospheric duct," *in Proc. ICC 2021-IEEE Int. Conf. Commun.*, pp. 1–6, Jun. 2021.

[17] B.-W. Shu, W.-S. Zhang, Y.-F. Chen, J. Sun, and C.-X. Wang, "Path loss prediction in evaporation ducts based on deep neural network," *IEEE Antennas Wirel. Propag. Lett.*, vol. 23, no. 2, pp. 798–802, Nov. 2024.

[18] S. Hochreiter and J. Schmidhuber, "Long short-term memory," *Neural Comput.*, vol. 9, pp. 1735–1780, 1997.

[19] J.-J. Wu, Z.-Q. Wei, J.-P. Zhang, X.-M. Guo, D.-N. Jia, J.-L. Xu, Y.-S. Zhang, Q.-L. Li, and H-Y. Zhou, "Environmental Knowledge-Driven Over-the-Horizon Propagation Loss Prediction Based on Short- and Long-Term Parallel Double-Flow TrellisNets," *IEEE Trans. Antennas Propagat.*, vol. 71, no. 12, pp. 9799–9813, Dec. 2023.

[20] H.-J. Ji, B. Yin, J. Zhang, Y. Zhang, Q. Li, and C. Hou, "Multiscale decomposition prediction of propagation loss for EM waves in marine evaporation duct using deep learning," *J. Mar. Sci. Eng.*, vol. 11, pp. 51, Sep. 2023.

[21] Y.-M. Wang and L. Wu, "On practical challenges of decomposition-based hybrid forecasting algorithms for wind speed and solar irradiation," *Energy*, vol. 112, pp. 208–220, Oct. 2016.

[22] K. Du, Y. Zhao and J. Lei, "The incorrect usage of singular spectral analysis and discrete wavelet transform in hybrid models to predict hydrological time series," *J. Hydrol.*, vol. 552, pp. 44–51, Sep. 2017.

[23] Z. Qian, Y. Pei, H. Zareipour, and N.-Y. Chen, "A review and discussion of decomposition-based hybrid models for wind energy forecasting applications," *Appl. Energy*, vol. 235, pp. 939–953, Feb. 2019.

[24] Y. Deng, B.-F. Wang and Z.-M. Lu, "A hybrid model based on data preprocessing strategy and error correction system for wind speed forecasting," *Energy Convers. Manage.*, vol. 212, pp. 1–24, May. 2020.

[25] A. Vaswani, N. Shazeer, N. Parmar, J. Uszkoreit, L. Jones, A. N. Gomez, L. Kaiser, and I. Polosukhin, "Attention is all you need," *in Proc. 31st Int. Conf. on Neural Inf. Process. Sys.*, pp. 6000–6010, Dec. 2017.

[26] B. R. Bean and E. J. Dutton, Radio meteorology. New York: Dover Publications, 1968.

[27] X.-M. Guo, D.-L. Zhao, L.-J. Zhang, H.-G. Wang, and S.-F. Kang, "A comparison study of sensitivity on PJ and NPS models in China seas," *J. Ocean Univ. China*, vol. 18, pp. 1022–1030, Aug. 2019.

[28] S. M. Babin and G. D. Dockery, "LKB-based evaporation duct model comparison with buoy data," *J. Appl. Meteorol.*, vol. 41, pp. 434–446, Apr. 2002.

[29] V. K. Ivanov, V. N. Shalyapin and Y. Levadnyi, "Determination of the evaporation duct height from standard meteorological data," *Izv. Atmos. Oceanic Phys.*, vol. 43, pp. 36–44, Feb. 2007.

[30] C. W. Fairall, E. F. Bradley, D. P. Rogers, J. B. Edson, and G. S. Young, "Bulk parameterization of air-sea fluxes for Tropical Ocean-Global Atmosphere Coupled-Ocean Atmosphere Response Experiment," *J. Geophys. Res.*, vol. 101, pp. 3747–3764, Feb. 1996.

[31] C. W. Fairall, E. F. Bradley, J. E. Hare, A. A. Grachev, and J. B. Edson, "Bulk parameterization of air-sea fluxes: updates and verification for the COARE algorithm," *J. Clim.*, vol. 16, pp. 571–591, Feb. 2003.

[32] R. A. Paulus, "Practical application of an evaporation duct model," *Radio Sci.*, vol. 20, pp. 887–896, Jul. 1985.

[33] R. Douvenot, V. Fabbro, C. Bourlier, J. Saillard, H. Fuchs, H. Essen, and J. Foerster, "Retrieve the evaporation duct height by least-squares support vector machine algorithm," *J. Appl. Remote Sens.*, vol. 3, pp. 033503–0335015, Jan. 2009.

[34] P. Gerstoft, L. T. Rogers, J. L. Krolik, and W. S. Hodgkiss, "Inversion for refractivity parameters from radar sea clutter," *Radio Sci.*, vol. 38, pp. 1–22, Jun. 2003.

[35] J. T. Saeger, N. G. Grimes, H. E. Rickard, and E. E. Hackett, "Evaluation of simplified evaporation duct refractivity models for inversion problems," *Radio Sci.*, vol. 50, pp. 1110–1130, Oct. 2015.

[36] X.-M. Guo, Q.-L. Li, Q. Zhao, S.-F. Kang, Y.-W. Wei and L.-X. Yang, "A comparative study of rough sea surface and evaporation duct models on radio wave propagation," *IEEE Trans. Antennas Propag.*, vol. 71, no .7, pp. 6060–6071, May. 2023.

[37] C. R. Sprouse and R. S. Awadallah, "An angle-dependent impedance boundary condition for the split-step parabolic equation method," *IEEE Trans. Antennas Propag.*, vol. 60, no.2, pp. 964–970, Oct. 2012.

[38] G. D. Dockery and J. R. Kuttler, "An improved impedance-boundary algorithm for Fourier split-step solutions of the parabolic wave equation," *IEEE Trans. Antennas Propag*, vol. 44, no. 12, pp. 1592–1599, Dec. 1996.

[39] J. R. Kuttler and G. D. Dockery, "Theoretical description of the parabolic approximation/Fourier split-step method of representing electromagnetic propagation in the troposphere," *Radio Sci.*, vol. 26, pp. 381–393, Mar. 1991.

[40] J. R. Kuttler and R. Janaswamy, "Improved Fourier transform methods for solving the parabolic wave equation," *Radio Sci.*, vol. 37, no. 2, pp. 1–11, Apr. 2002.

[41] Z. Qiu, C. Zhang, B. Wang, T. Hu, J. Zou, Z. Li, S. Chen, and S. Wu, "Analysis of the accuracy of using ERA5 reanalysis data for diagnosis of evaporation ducts in the East China Sea," *Front. Mar. Sci.*, vol. 9, pp. 1–14, Jan. 2023.

[42] O. A. Alduchov and R. E. Eskridge, "Improved Magnus form approximation of saturation vapor pressure," *J. Appl. Meteorol.*, vol. 35, no. 4, pp. 601–609, Apr. 1996.

[43] M. G. Lawrence, "The relationship between relative humidity and the dewpoint temperature in moist air: a simple conversion and applications," *Bull. Am. Meteorol. Soc.*, vol. 86, no. 2, pp. 225–233, Feb. 2005.

[44] J.-P. Zhang, Y.-S. Zhang, X.-Y. Xu, Q.-L. Li, and J.-J. Wu, "Estimation of sea clutter inherent Doppler spectrum from shipborne S-band radar sea echo," *Chin. Phys. B*, vol. 29, no. 6, pp. 68402, Jun. 2020.

[45] X.-M. Guo, D.-L. Zhao, L.-J. Zhang, H.-G. Wang, S.-F. Kang, and L.-K. Lin, "C band transhorizon signal characterisations in evaporation duct propagation environment over Bohai Sea of China," *IET Microwaves Antennas Propag*, vol. 13, no. 4, pp. 407–413, Feb. 2019.

[46] W.-P. Zhao, J. Zhao, J.-C. Li, D.-D. Zhao, L.-L. Huang, J.-X. Zhu, J.-Z. Lu, and X. Wang, "An evaporation duct height prediction model based on a long short-term memory neural network," *IEEE Trans. Antennas Propag*, vol. 69, no. 11, pp. 7795–7804, May. 2021.

[47] D. Zhu, P. Zhao, Q. Zhao, Q.-L. Li, Y.-S. Zhang, and L.-X. Yang, "A two-stream LSTM-based backscattering model at L-band and S-band for dry soil surfaces under large roughness conditions," *IEEE J. Sel. Top. Appl. Earth Obs. Remote Sens.*, vol. 17, pp. 3137–3150, Dec. 2024.

Hanjie Ji received the M.S. degree in electronic information from the Ocean University of China, Qingdao, China, in 2023. He is currently pursuing the Ph.D. degree in radio physics at School of Physics, Xidian University.

His research interests include radio wave propagation, atmospheric duct, machine learning, and remote sensing.

Lixin Guo (Senior Member, IEEE) received the M.S. degree in radio science from Xidian University, Xi'an, China, in 1993, and the Ph.D. degree in astrometry and celestial mechanics from the Chinese Academy of Sciences, Beijing, China, in 1999. He has authored or coauthored six books and over 300 journal articles. He has been in charge of and undertaken more than 30 projects.

His research interests include radio wave propagation and scattering in complex and random media, computational electromagnetics, inverse scattering, and antenna analysis and design.

Jinpeng Zhang received the Ph.D. degree in radio physics from Xidian University, Xi'an, China, in 2013. He is currently a Researcher with the China Research Institute of Radiowave Propagation, Qingdao, China.

He is mainly engaged in the research of electromagnetic scattering and sea clutter characteristics.

Yiwen Wei (Member, IEEE) received the B.S. degree in electronic information and technology and the Ph.D. degree in radio physics from Xidian University, Xi'an, China, in July 2010 and June 2016, respectively. She is currently an Associate Professor with the School of Physics, Xidian University.

Her research interests include radio wave propagation and scattering in complex systems, SAR images, and remote sensing.

Xiangming Guo received the M.S. degree in electromagnetic field and microwave technology from the China Research Institute of Radiowave Propagation, Qingdao, China, in 2009, and the Ph.D. degree in physics oceanography from the Ocean University of China, Qingdao, in 2019. He is currently a Senior Engineer with the China Research Institute of Radiowave Propagation, Qingdao, China.

His research interests include radio wave propagation and atmospheric duct.

Yusheng Zhang received the B.S. degree from the Nanjing University of Information Science & Technology, Nanjing, China, in 1992. He is currently a Researcher with the China Research Institute of Radiowave Propagation, Qingdao, China.

His research interests include radio wave environmental characteristics and atmospheric numerical simulation.

Tianhang Nie received the B.S. degree from Xidian University, Xi'an, China, in 2022. He is currently pursuing the M.S. degree with Xidian University, Xi'an, China.

His research interests include atmospheric duct, radio wave propagation and scattering.

Jie Feng received the M.S. degree in radio physics from the China Research Institute of Radiowave Propagation, Qingdao, China, in 2016. She is currently a Senior Engineer with the China Research Institute of Radiowave Propagation, Qingdao, China.

Her research interests include Space plasma, dust plasma, and electromagnetic wave propagation.